catalysts

MDPI

Article

Performance of Mn-Fe-Ce/GO-x for Catalytic Oxidation of Hg^0 and Selective Catalytic Reduction of NO_x in the Same Temperature Range

Donghai An, Xiaoyang Zhang, Xingxing Cheng * and Yong Dong *

National Engineering Lab for Coal-fired Pollutants Emission Reduction, Shandong University, Jinan 250061, China; adhcjxy@163.com (D.A.); angxiaoang2014@163.com (X.Z.)

* Correspondence: xcheng@sdu.edu.cn (X.C.); dongy@sdu.edu.cn (Y.D.); Tel.: +86-0531-883-99370 (Y.D.)

Received: 28 July 2018; Accepted: 11 September 2018; Published: 18 September 2018

Abstract: A series of composites of Mn-Fe-Ce/GO-x have been synthesized by a hydrothermal method. Their performance in simultaneously performing the catalytic oxidation of Hg^0 and the selective catalytic reduction of nitrogen oxides (NO_x) in the same temperature range were investigated. In order to investigate the physicochemical properties and surface reaction, basic tests, including Brunauer-Emmett-Teller (BET), XRD, scanning electron microscope (SEM) and X-ray photoelectron spectroscopy (XPS) were selected. The results indicate that the active components deposited on graphene play an important role in the removal of mercury and NO_x, with different valences. Especially, the catalyst of Mn-Fe-Ce/GO-20% possesses an excellent efficiency in the temperature range of 170 to 250 °C. Graphene has a huge specific surface area and good mechanical property; thus, the active components of the Mn-Fe-Ce catalyst can be highly dispersed on the surface of graphene oxide. In addition, the effects of O_2, H_2O, NO and SO_2 on the removal efficiency of Hg^0 were examined in flue gas. Furthermore, the regeneration experiments conducted by thermal methods proved to be promising methods.

Keywords: mercury removal; NO_x removal; Mn-Fe-Ce/GO-x; same temperature range

1. Introduction

In recent years, the removal of mercury and its derivatives has attracted significant attention due to their toxic effects on ecological safety and human health [1–3]. Many researchers have explored an effective way to control the emission of mercury from coal-fired power plants. As we know, mercury is released into exhaust gas in the form of elemental mercury (Hg^0), oxidized mercury (Hg^{2+}) and particulate bound mercury (Hg^p) [4–6]. At present, Hg^2+ is water-soluble and can be easily removed by wet flue gas desulfurization, and Hg^p attached to fly ash can be captured by electrostatic precipitators and fabric filters. In a word, Hg^{2+} and Hg^p can easily be controlled by existing air pollution control devices [7–12]. However, Hg^0 is difficult to capture due to its high volatility and water-insolubility. Therefore, Hg^0 is the main mercury species that is emitted in the stack flue gas from coal-fired utilities. Even more alarming, Hg^0 can circulate in the atmosphere for years, and its toxic effects have a global-scale impact. Consequently, the conversion of Hg^0 to Hg^{2+} or Hg^p is the main method of removing elemental mercury. In previous explorations, methods of sorbent injection, catalytic oxidation, electrocatalytic oxidation, and photochemical oxidation were carried out to remove Hg^0 [13–18]. Therein, the catalytic oxidation of Hg^0 is the most promising method due to its high-efficiency.

Besides the difficulties that are associated with mercury removal, reducing the emission of NO_x is also difficult. NO_x from the exhaust gases of coal-fired power plants is the major source of air pollution.

Specifically, NO_x causes photochemical smog, acid rain, ozone depletion, and greenhouse effects, etc. So far, the commercial catalyst of V_2O_5-WO_3/TiO_2 is widely used in the field of controlling NO_x emission. However, this catalyst is significantly affected by the flue gas temperature and easily loses its catalytic activities at low temperatures. Meanwhile, the addition of chlorine into the boiler is needed in order to realize the activities of Hg^0 oxidation [19–21]. It is necessary to explore an effective and economical catalyst to remove Hg^0 and NO_x in the same temperature range, without the assistance of chlorine.

Besides the V_2O_5-WO_3/TiO_2 catalyst, many transition metal oxides were explored for the oxidation of Hg^0 and the reduction of NO_x, such as MnO_x, FeO_x, CeO_x, V_2O_5, CuO_x and CoO_x [22–25]. However, the single metal oxides, as mentioned above, can hardly meet the demand of simultaneously removing Hg^0 and NO_x. Hence, researchers tried to dope one or more metal oxides to obtain catalysts with a higher performance. For instance, Mn-Ce/TiO_2, Mn-Fe spinel and Ce-Fe-O were studied to enhance the performance of a single metal oxide for Hg^0 and NO_x removal [26–28]. Mn-Ce/TiO_2 is highly effective in removing Hg^0 and NO_x, for the reason that the Mn oxides exhibit excellent catalytic activities at lower temperatures, and the Ce oxides can provide an amount of trapped oxygen for redox [29–31]. However, its high performance is inhibited by SO_2 in the flue gas. In order to explore the catalyst that is resistant to SO_2, Mn-Fe spinel has been explored, which possesses an excellent SO_2-resistance ability, by doping Mn oxides with Fe oxides. Regrettably, the Hg^0 oxidation ability of Mn-Fe spinel is limited. It is necessary to explore a catalyst that possesses inhibitory effects of SO_2 and a high activity under different flue gas conditions. The above problems motivate us to focus on the design and synthesis of new catalysts with an optimal catalytic performance. To the best of our knowledge, using the three metal oxides, MnO_x, CeO_x, and FeO_x, to synthesize the Fe-Mn-Ce oxide-based catalyst has seldom been reported in the literature for Hg^0 oxidation and NO_x reduction [32]. Thus, we carried out systematic explorations on the Fe-Mn-Ce oxide-based catalyst.

Moreover, the carrier plays an important role in enhancing the performance of the catalyst. Usually, the metal oxides have a small specific surface area, while the carrier has a big specific surface area. In particular, graphene is a planar sheet that is composed of carbon atoms [33–35]. Its large surface area (calculated value, 2630 m^2/g) is convenient for the dispersion of active components. Moreover, the mobility of charge carriers (200,000 cm^2/Vs) can significantly facilitate electron transfer in an oxidation-reduction reaction [31]. According to the literature, graphene can be oxidized by strong acid or other methods to obtain graphene oxide (GO) with many functional groups, which can offer abundant nucleation sites for metal atoms. It is a viable approach to exploring new catalysts, while using GO as a catalyst carrier.

In this work, the Mn-Fe-Ce/GO-x catalysts were synthesized via a hydrothermal method, based on the excellent properties of GO as a catalyst carrier. Moreover, the characterization methods of Brunauer-Emmett-Teller (BET), XRD, scanning electron microscope (SEM), and X-ray photoelectron spectroscopy (XPS) were selected to reveal the physicochemical properties of the Mn-Fe-Ce/GO-x catalysts. The composites were investigated through a fixed-bed reaction system for Hg^0 and NO_x removal in the temperature range of 100 to 400 °C. Moreover, the effects of flue gas components, including O_2, NO, H_2O and SO_2, on the oxidation of Hg^0 and reduction of NO_x were discussed. The combination of GO sheets and the Mn-Ce-Fe-O particles is advantageous for the application of Mn-Ce-Fe oxides. The outstanding performance was discussed in light of the test results and characterization techniques.

2. Results and Discussion

2.1. Characterization of Catalysts

The microstructural parameters of Ce-Mn-Fe/GO-x (x = 0, 10%, 20%, 30%) catalysts were investigated, and the results are listed in Table 1. With the increase of GO content from 0 to 20%, the specific surface area, pore volume and pore diameter of the catalysts correspondingly increased

from 2.37 to 109.23 m^2/g, 0.0089 to 0.0462 cm^3/g, and 2.321 to 3.426 nm, respectively. However, further increasing the GO content to 30% resulted in a decrease of microstructural parameters due to the aggregation of GO. Therefore, the Ce-Fe-Mn/$GO_{0.2}$ with an appropriate carrier of GO is considered to be a candidate with a better catalytic performance.

Table 1. Microstructural parameters of Ce-Mn-Fe/GO-x (x = 0, 10%, 20%, 30%).

Samples	BET Surface (m^2/g)	Pore Volume (cm^3/g)	Average Pore Diameter (nm)
Ce-Mn-Fe/GO-0	2.37	0.0089	2.321
Ce-Mn-Fe/GO-10%	54.39	0.0363	3.418
Ce-Mn-Fe/GO-20%	109.23	0.0463	3.426
Ce-Mn-Fe/GO-30%	79.95	0.0395	3.415

The XRD patterns of Ce-Mn-Fe/GO-x (x = 0, 10%, 20%, 30%) catalysts are shown in Figure 1. All of the samples show characteristic diffraction peaks of MnO_2 and Mn_3O_4 in the patterns. Nevertheless, few weak peaks of crystalline Fe and Ce oxides are detected in the XRD patterns, indicating that all the Fe and Ce oxides have a fine grain size and exist in an amorphous form. The characteristic diffraction peaks of graphene, at approximately 20–25° in the results, are found in Ce-Mn-Fe/GO-x (x = 10%, 20%, 30%), suggesting that the graphene structure was successfully synthesized, and the peak of GO, at approximately 2θ = 13°, is also detected by a Bruker D2 PHASER diffractometer.

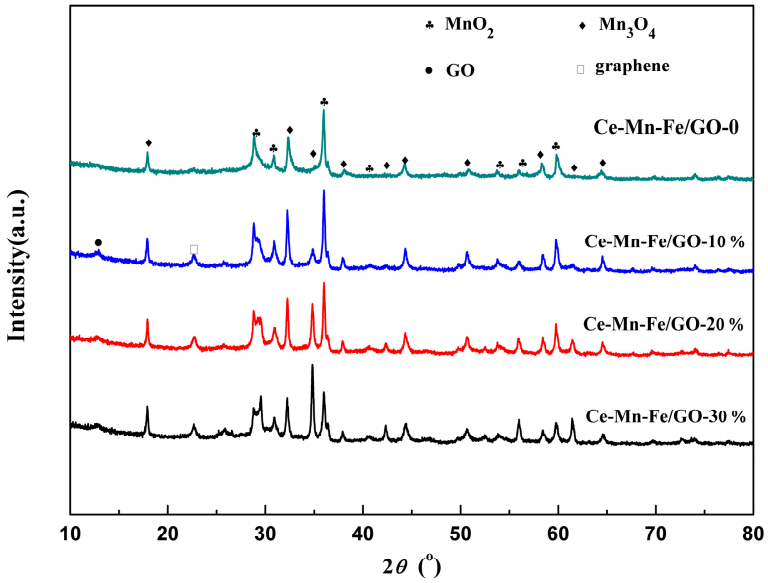

Figure 1. The XRD patterns of Ce-Mn-Fe/GO-x (x = 0, 10%, 20%, 30%).

In order to further identify the composition and content on the surface of all the samples, the EDS of Ce-Mn-Fe/GO-20% was selected, and the results are shown in Figure 2. Ce-Mn-Fe/GO-0, Ce-Mn-Fe/GO-10% and Ce-Mn-Fe/GO-30% are shown in Figures S1–S3 in the Supporting Information, respectively. It can be seen, from all of these Figures, that the catalysts present the contents of Fe, Ce, Mn and O elements on the GO carrier. That is to say, there were no visible phases of Fe and Ce oxides in the XRD patterns, indicating that all of the Fe and Ce oxides were highly dispersed over the support, with a low content. The EDS proves the existence of Fe and Ce oxides on GO.

The SEM characterization provides a convenient approach to investigating the morphology of the prepared catalysts. Images of microscopic Ce-Mn-Fe/GO-0 and Ce-Mn-Fe/GO-10% morphologies, which are particle-like as well as highly aggregated and disorganized, are shown in Figures S1 and S2. As shown in the image of Ce-Mn-Fe/GO-20% in Figure 2, the metal oxides distributed on the GO structure were more uniform and showed a smaller particle size. Ce-Mn-Fe/GO-30% in Figure S3

indicates that plenty of GO join together to limit the attachment of oxides, and this result is consistent with the BET test. In the catalyst of Ce-Mn-Fe/GO-20%, numerous nanoparticles were inserted into the GO sheets for further analysis, and this result indicates that GO can not only prevent the aggregation of catalytic activity particles, but also the nanoparticles load on GO through functional groups, such as carboxyl, hydroxyl, and epoxy groups [36]. Hence, the highly dispersed and uniform nanoscale Ce-Mn-Fe-O particles are embedded in GO.

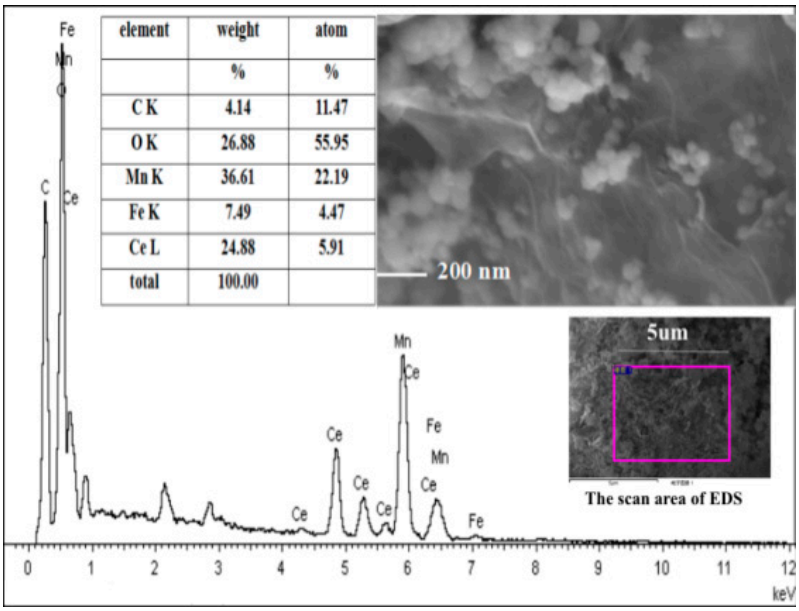

Figure 2. The element contents on the surface of graphene oxide (EDS) and scanning electron microscope (SEM) images of Ce-Mn-Fe/GO-20%.

The XPS spectra of the samples were performed to further illustrate the chemical composition and the valence states of Mn, Ce and Fe. The results are exhibited in Figure 3, the Mn 3d spectra with two main peaks, corresponding to Mn $2p_{3/2}$ and Mn $2p_{1/2}$, are observed in Figure 3a. The Mn $2p_{1/2}$ peak consists of three sub-peaks, the corresponding binding energy of Mn^{3+} is 641.8 eV, and the peaks at about 642.4 eV, 641.2 eV, and 640.2 eV are Mn^{4+}, Mn^{3+} and Mn^{2+}, respectively. The rate of $(Mn^{4+} + Mn^{3+})/Mn^{2+}$ was usually considerable for Hg^0 oxidation, based on article [37]. The high valence Mn oxides enhance Hg^0 oxidation efficiency, as Mn^{4+} can directly oxidize the adsorbed Hg^0, and Mn^{3+} also has potential activity in Hg^0 oxidation in the presence of O_2. Manganese oxides exist at the mixed states of Mn^{4+} and Mn^{3+} in the four composition catalysts of Ce-Mn-Fe/GO-x (x = 0, 10%, 20%, 30%). In particular, the Ce-Mn-Fe/GO-20% possesses a higher Hg^0 oxidation efficiency than other catalysts of Ce-Mn-Fe/GO-x (x = 0, 10%, 30%), and the main reason may be that the highest ratios of $(Mn^{4+} + Mn^{3+})/Mn^{2+}$ are in the Ce-Mn-Fe/GO-20% sample, which plays an important role in Hg^0 oxidation. In addition, the catalyst has quite a high content of Mn^{4+} and Mn^{3+} on the surface and it shows good activity in NO_x reduction with NH_3 at low temperatures [38].

The XPS spectra of Ce3d for these catalysts are presented in Figure 3b. The peaks that were labeled U and V were the corresponding $3d_{5/2}$ and $3d_{3/2}$ spin-orbit states, respectively [39]. The U_0, U_1, U_3, V_3, V_2, and V_0 belonged to the $3d^{10}4f^0$ state of the Ce^{4+} species, and U_2 and V_1 are assigned to the $3d^{10}4f^1$ initial electronic state of the Ce^{3+} species [40]. When comparing with the four catalysts, the Ce-Mn-Fe/GO-10% has the highest ratio of Ce^{4+}/Ce^{3+}, but the ratio of Ce^{4+}/Ce^{3+} decreases in the optimal catalyst, Ce-Mn-Fe/GO-20%, and it can be inferred from this result that some reactions take place in the preparation process. Thus, the most possible reaction is as follows [41]:

$$2CeO_2 + Mn_2O_3 \rightarrow Ce_2O_3 + 2MnO_2 \quad (1)$$

The reaction further explains the reason why the Ce-Mn-Fe/GO-20% has high ratios of $(Mn^{4+} + Mn^{3+})/Mn^{2+}$. The ratios of Ce^{4+}/Ce^{3+} were calculated and are shown in Figure 3b, and it is obvious that the majority of the Ce ions are Ce^{4+}, which is beneficial for Hg^0 oxidation. Moreover, it has been reported that the Ce^{3+} species can not only create charge imbalance, vacancies, and unsaturated chemical bonds, but also enhance Hg^0 oxidation with the chemisorbed oxygen species on the surface of catalyst [42].

The XPS spectra of Fe2p for catalysts are shown in Figure 3c. The peaks appeared at 709.3 eV, which was attributed to Fe^{2+} cations [43], and at the 711.42 eV, 713.2 eV, 725.4 eV, which were assigned to Fe^{3+}. Different states of iron cations contain a weak oxidation property in relation to Hg^0, however, they have positive effects on NO_x reduction with NH_3 at the ideal temperatures [44].

As shown in Figure 3d, the peaks at low binding energy (about 259.5–25.97 eV) could be regarded as lattice oxygen (denoted as O_α), the binding energy peak at 531.0–531.7 eV is attributed to chemisorbed oxygen and C=O groups (denoted as O_β), and the peak at 532.7–533.5 eV was reported to exist in hydroxy (denoted as O_r) [45,46]. When comparing GO with Ce-Mn-Fe/GO-0, the peaks at about 532.8–533.5 eV belong to GO, however, the peaks at about 259.5–25.97 eV belong to the metal oxide nanocrystals. On the Ce-Mn-Fe/GO-x (10%, 20%, 30%), the peaks at 531.1–531.7 eV may belong to GO and metal oxide. In this study, the concentrations of the three types of O were listed in Table 2. The concentration of O_β and O_r on the GO is 45.36% and 54.64%, respectively. On the Ce-Mn-Fe/GO-0, the concentration of O_α and O_β is 60.24% and 30.76%, respectively. With the increasing of GO content from 0.1 to 0.3, the intensity percentage of O_β on Ce-Mn-Fe/GO-x (10%, 20%, 30%) is 31.73%, 32.16%, and 18.4%, respectively. The catalyst of Ce-Mn-Fe/GO-20% has a higher efficiency of Hg^0 removal than Ce-Mn-Fe/GO-x (20%, 30%), because the O_β species are believed to be the most active oxygen for oxidation reactions [47].

Table 2. The concentrations of different types of oxygen (O_α, O_β, O_r) in graphene oxide (GO) and Ce-Mn-Fe/GO-x (x = 0, 10%, 20%, 30%).

Sample	Surface Atomic Concentrations (%)		
	O_α	O_β	O_r
GO	0	45.36	54.64
Ce-Mn-Fe/GO_0	60.24	30.76	0
Ce-Mn-Fe/$GO_{0.1}$	61.65	31.73	6.62
Ce-Mn-Fe/$GO_{0.2}$	59.89	32.26	7.85
Ce-Mn-Fe/$GO_{0.3}$	66.89	18.40	14.70

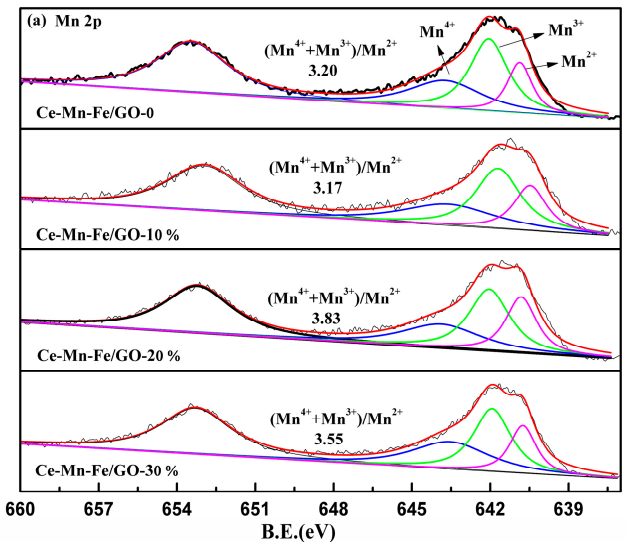

Figure 3. *Cont.*

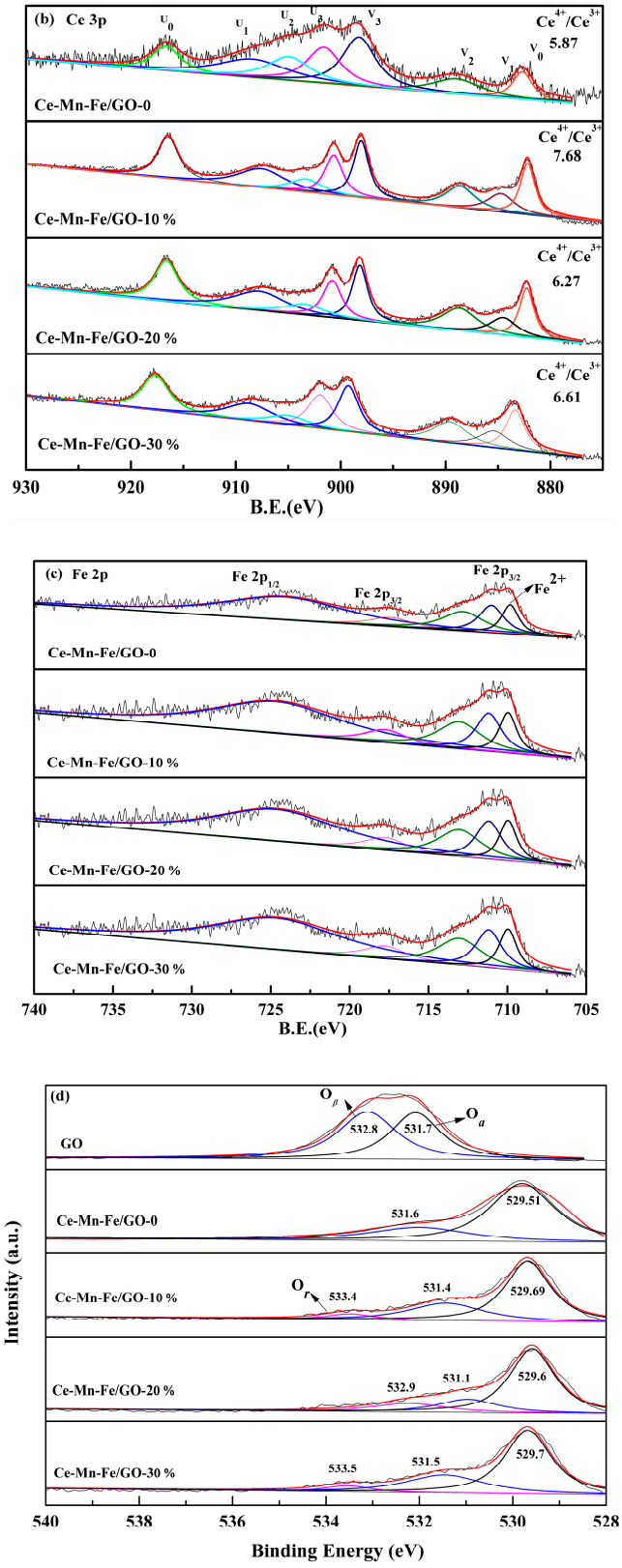

Figure 3. X-ray photoelectron spectroscopy (XPS) spectra of Mn 2p (**a**), Ce 3p (**b**), Fe 2p (**c**) and O 1s (**d**) for Ce-Mn-Fe/GO-x (x = 0, 10%, 20%, 30%).

As discussed above, the reactive temperatures of Hg^0 shift to a low temperature region when the manganese oxides are involved in the reaction. The cerium has a superior ability to store oxygen,

which contributes to Hg^0 oxidation and NO_x reduction. The oxidizability of manganese and cerium oxides is stronger than that of iron oxides, and the presence of the iron content can enhance the high valence states of the other two metal oxides [33]. As the result, the catalysts that contain the three metals show an effective property for Hg^0 and NO_x removal.

The reducibility of the prepared catalysts of Ce-Mn-Fe/GO-x (x = 0, 10%, 20%, 30%) was detected by H_2-TPR in the temperature range of 100–900 °C, and the results are shown in Figure 4. For Ce-Mn-Fe/GO-0, the peak at around 314 °C can be attributed to the reduction of a highly dispersed MnO_2 to Mn_3O_4. In addition, the higher two reduction peaks at 422 and 494 °C are the reductions of Mn_2O_3 to MnO and Fe_3O_4 to FeO, respectively [30,48]. The peak at 678 °C may be a reduction of CeO_2 to Ce_2O_3 [49]. The peak above 750 °C was assigned to the reduction of surface FeO to Fe [50]. The sample of Ce-Mn-Fe/GO-10% shows three apparent peaks in the H_2-TPR curves, and the reduction When compared with Ce-Mn-Fe/GO-10%, the reduction peaks of Ce-Mn-Fe/GO-20% shift to a lower temperature due to the increase of GO. Furthermore, Ce-Mn-Fe/GO-30% evidently has an increase in GO, and the reduction curves shift gradually towards a higher temperature, the main reason being that amounts of GO join together and lead to a decrease of reducibility of metallic oxides. Above all, the sample of Ce-Mn-Fe/GO-20% has higher redox ability, with moderate GO.

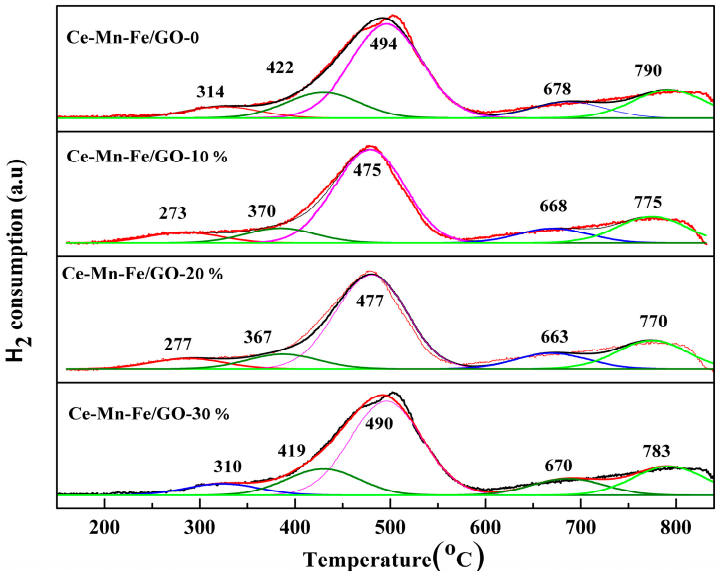

Figure 4. TPR profiles of the Ce-Mn-Fe/GO-x (x = 0, 10%, 20%, 30%) samples.

2.2. The Performance of the Prepared Materials

The Hg^0 oxidation and NO_x recondition efficiencies over Ce-Mn-Fe/GO-x (x = 0, 10%, 20%, 30%) were studied at reaction temperatures, with a range of 100 to 400 °C, and the results are shown in Figure 5. The catalysts of Ce-Mn-Fe/GO-x (x = 0, 10%, 20%, 30%) exhibit weak E_{oxi}, which is approximately 30%, 43%, 67%, and 45% at 100 °C, respectively. The efficiency at this temperature is mainly attributed to the physical adsorption and oxidation of O_β on the surface of Ce-Mn-Fe/GO-x (x = 0, 10%, 20%, 30%) for Hg^0 oxidation. The E_{oxi} increases with the increasing of temperature, and over 95% of E_{oxi} can be obtained at 170 °C for Ce-Mn-Fe/GO-20% and Ce-Mn-Fe/GO-30%. However, the value for Ce-Mn-Fe/GO-30% starts to decrease, when the temperature reaches 200 °C, and it continues to reduce in the range of 200 to 400 °C. Ce-Mn-Fe/GO-20% maintains the highest E_{oxi}, until the temperature reaches 250 °C, at which point it decreases rapidly until 400 °C. The samples of Ce-Mn-Fe/GO-0 and Ce-Mn-Fe/GO-10% exhibit the highest E_{oxi}, exceeding 87% at 300 °C and 83% at 220 °C, and the E_{oxi} decreases to about 62% and 22% at 400 °C, respectively. Comparing the four composites in relation to E_{oxi}, the sample of Ce-Mn-Fe/GO-20% shows an outstanding efficiency with a low temperature of 170 °C and when the temperature span is 80 °C (see the larger image in Figure 5).

The reason is that metallic oxide particles uniformly load on GO with a large specific surface area, which is beneficial for Hg^0 absorption and oxidation.

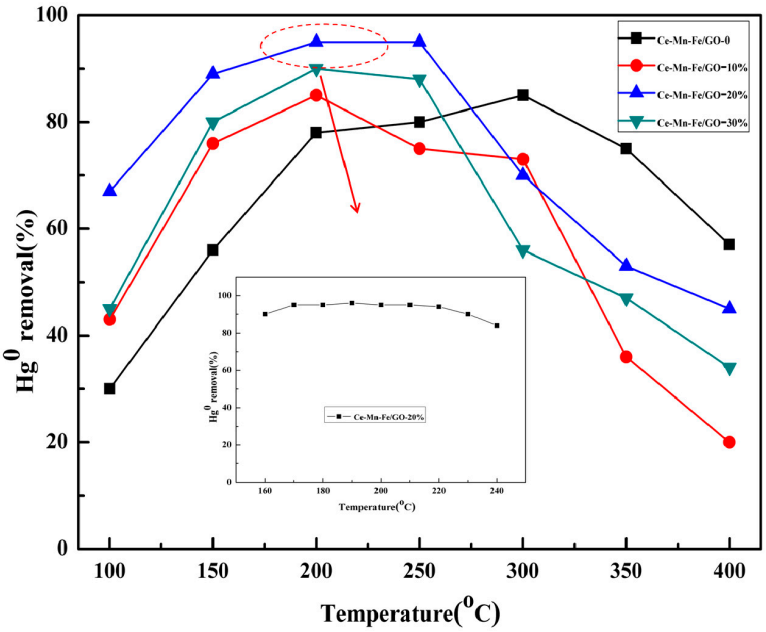

Figure 5. Hg^0 removal over Ce-Mn-Fe/GO-x (x = 0, 10%, 20%, 30%) catalysts at different temperatures (Flue gas conditions: 6% O_2, 600 ppm SO_2, 800 ppm nitrogen oxide (NO), N_2 as balance gas).

The η of Ce-Mn-Fe/GO-20% at different temperatures with NH_3 is shown in Figure 6. At the reaction temperature of 160 to 255 °C (see the larger image in Figure 6), the η is maintained at above 90%, indicating that the catalyst has a rather wide temperature window. Especially, the η reaches 97% at 170 °C. Interestingly, the excellent E_{oxi} and η of Ce-Mn-Fe/GO-20% is exhibited in the same temperature range of 170–250 °C, and the highest efficiencies that can be achieved are 95% and 97%, respectively. The η over Ce-Mn-Fe/GO-0, Ce-Mn-Fe/GO-10%, and Ce-Mn-Fe/GO-30% catalysts were also investigated, and the results are shown in the Supporting Information for comparison (Figure S4).

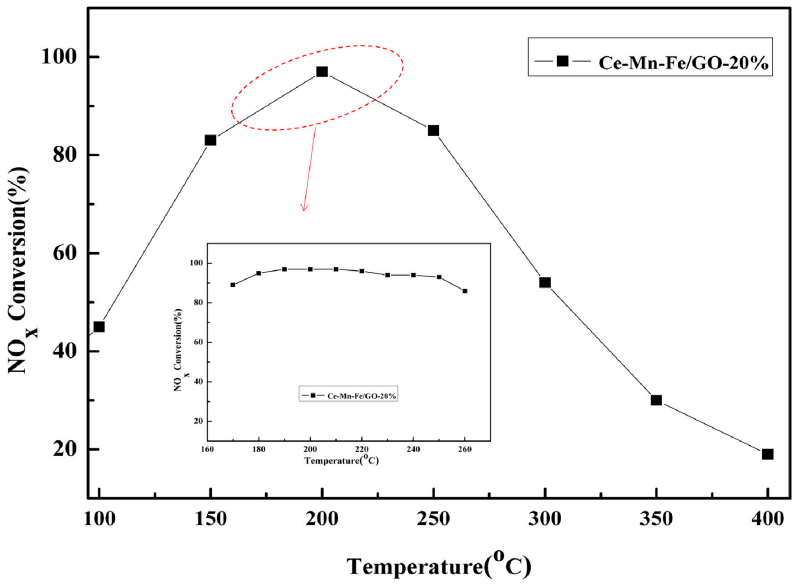

Figure 6. NO_x conversion as a function of reaction temperature over the Ce-Mn-Fe/GO-20% sample. (Flue gas conditions: 6% O_2, 600 ppm SO_2, 800 ppm NO, 800 ppm NH_3, N_2 as balance gas).

The N_2O output concentration over Ce-Mn-Fe/GO-20% is shown in Figure 7a. This shows that nearly 100% N_2 selectivity was obtained in the region of 180–250 °C over the catalysts. However, the N_2O output concentration over Ce-Mn-Fe/GO-20% gradually increased with the rising temperature in the region of 280–300 °C, due to the produce of N_2O, resulting from the gradual oxidation of NH_3 at a high temperature. The changes of NO_2 concentration in the region of 140–300 °C, indicating that there is almost no NO_2 output, as shown in Figure 7b.

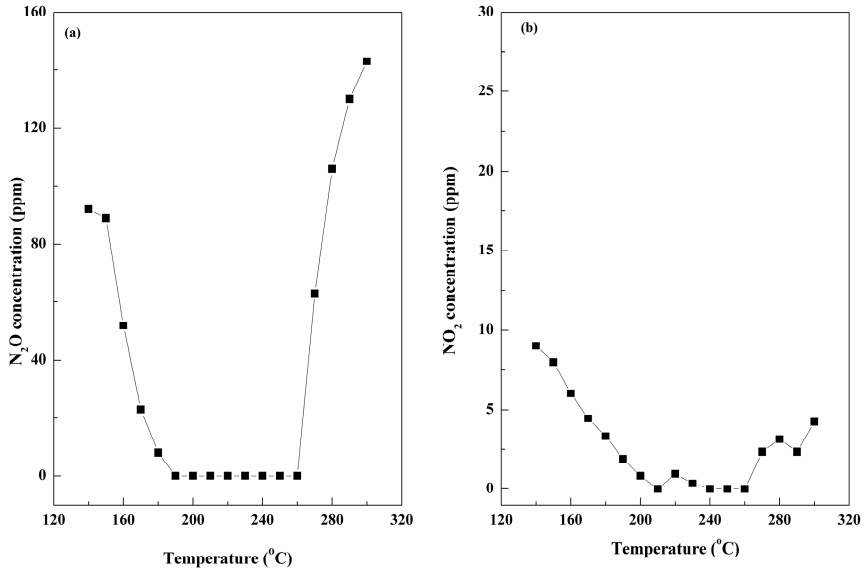

Figure 7. The N_2O output concentration (**a**), NO_2 output concentration (**b**) over Ce-Mn-Fe/GO-20%.

2.3. Effect of Individual Flue Gas Components

Hg^0 oxidation efficiencies (average value of one hour) over the Ce-Mn-Fe/GO-20% catalyst at 170 °C, under different flue gas components, are shown in Figure 8.

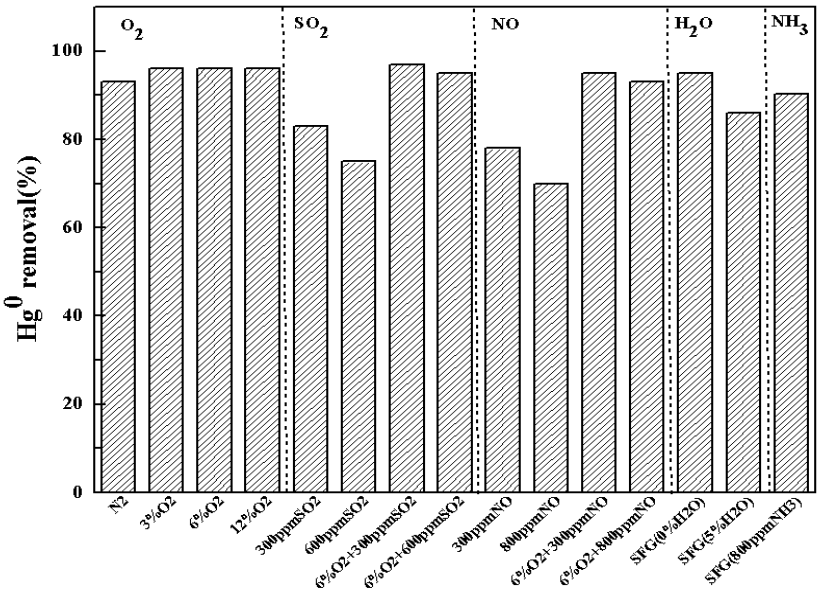

Figure 8. Effect of the flue gas components on Hg^0 removal over the Ce-Mn-Fe/GO-20% sample at 170 °C.

2.3.1. The Effect of O_2 on Mercury Oxidation over the Ce-Mn-Fe/GO-20% Catalyst

O_2 plays an important role in Hg^0 oxidation and NO_x reduction, and the results are presented in Figure 8. In the absence of O_2 (pure N_2), at first, the E_{oxi} is 93%, but after a time, the E_{oxi} decreases. When the O_2 concentration increases to 3%, the Hg^0 removal performance is enhanced, and E_{oxi} is 96%. To further investigate the effect of O_2 on Hg^0 oxidation, 6% O_2 was added in the simulated flue gas, and the E_{oxi} is increased to 98%. A further increase to 12% O_2 makes no sense. Obviously, O_2 is favorable for Hg^0 oxidation, and this is in accordance with previous studies [23].

2.3.2. The Effect of SO_2 on Mercury Oxidation over the Ce-Mn-Fe/GO-20% Catalyst

The effect of SO_2 on E_{oxi} includes inhibition, promotion, and non-response. In our study, different concentrations of SO_2 (300 ppm and 600 ppm SO_2) were added into the pure N_2 gas flow, and the result is demonstrated in Figure 8. The E_{oxi} decreases from 93% (pure N_2) to 83% and 75%, with an SO_2 concentration gradient of between 300 ppm to 600 ppm. SO_2 has an inhibition effect on mercury removal. Besides, 6% O_2 and 300 ppm SO_2 were added to the mixer, interestingly increasing the E_{oxi} to 97%, and the result changes little when the concentration of SO_2 changes from 300 ppm to 600 ppm. The reason is that the SO_2 may not only directly react with O_2 over the catalyst, but may also react with the lattice oxygen to form SO_3, which can offer more acid active sites to oxidize the adsorbed Hg^0 [51].

2.3.3. The Effect of NO on Mercury Oxidation over the Ce-Mn-Fe/GO-20% Catalyst

The affecting factor of NO concentration is usually considered in relation to Hg^0 removal. In this study, the selected concentrations of NO were 300 ppm and 800 ppm. As shown in Figure 8, in the absence of NO, pure N_2 was used for comparison, in which the E_{oxi} is 93%. In an atmosphere of 300 ppm and 800 ppm NO, the E_{oxi} is 78% and 70%, respectively, and the NO exhibits an inhibitory effect on Hg^0 removal. In addition, the E_{oxi} increased to 95% and 92% when 6% O_2 was added to 300 ppm and 800 ppm NO. The probable reason for the promotional effect is that NO could be oxidized by the surface oxygen species in order to generate active species, such as NO_2 [52]. Therefore, a promotional effect of NO with O_2 on mercury removal in this study was attributed to the production of NO_2, which can provide acid sites on the catalyst surface.

2.3.4. The Effect of Water Vapor on Mercury Oxidation over the Ce-Mn-Fe/GO-20% Catalyst

Under the simulated flue gas (SFG), the E_{oxi} is 98.6% (0% H_2O) and the effect of water vapor on Hg^0 oxidation was explored. The result is shown in Figure 8, in which it can be seen that the water vapor exhibits an inhibitory effect on Hg^0 oxidation. The 5% water vapor was added to the simulated flue gas. The E_{oxi} decreases from 98.6% to 81.3%, which is probably due to the existence of water on the active sites available for mercury adsorption [53]. Fortunately, the catalyst has better properties of water resistance when compared with others (Ce-Mn-Fe/GO-0, Ce-Mn-Fe/GO-10% and Ce-Mn-Fe/GO-30%). Hence, the catalyst has a potential application in the humid flue gas environment. Besides, the effect of NH_3 on Hg^0 removal was investigated, and adding 800 ppm NH_3 to the SFG caused the E_{oxi} to decrease slightly. NO should be considered because NO reacts with NH_3 over the catalyst, and NH_3 displays a slight inhibitory effect on Hg^0 removal.

2.4. Effect of Individual Flue Gas Components on NO_x Removal over the Ce-Mn-Fe/GO-20% Catalyst under NH_3

Additionally, the effects of SO_2 and H_2O have been explored, under operating conditions, on NO_x removal, and the results were demonstrated in Figure 9. SO_2 has an adverse effect on NO_x removal when 300 ppm SO_2 is included in the simulated flue gas (SFG), and η decreased from 97% to 83% and further decreased to 78% when the concentration of SO_2 increased to 600 ppm. Then, cutting off SO_2, the efficiency recovered slightly. The main reason is that the SO_2 can combine with NH_3 to form ammonium sulfate and cover the surface of the catalyst to inhibit the reaction, resulting in a

decrease of catalytic activity. Water vapor presented an inhibitive effect on η over Ce-Mn-Fe/GO-20% when 6% of water vapor was added to the simulated flue gas, and η gradually decreased from 97% to 83%. The competitive adsorption between H_2O and NH_3 on the surface of the catalyst could account for the deactivation [54]. It is worth noting that the conversion can recover soon after cutting off the H_2O injection.

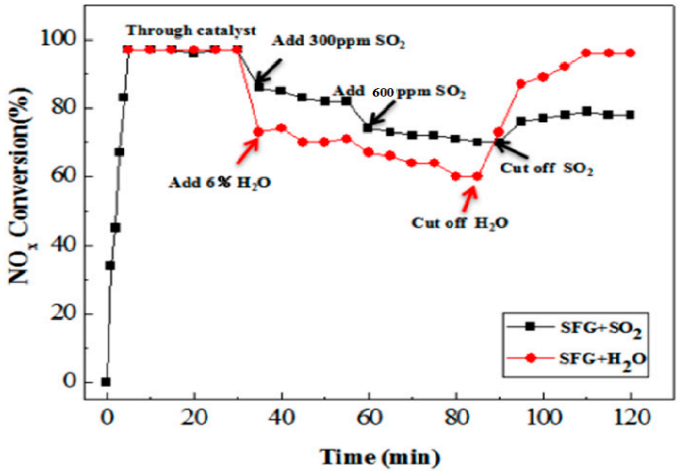

Figure 9. The influence of SO_2 and H_2O on de-NO_x performance over the Ce-Mn-Fe/GO-20% sample.

2.5. Proposed Hg^0 Oxidation Mechanism

The adsorption mechanism of Hg^0 can be described by the following reactions [55]:

$$Hg^0(g) + Surface \rightarrow Hg(ad) \quad (2)$$

$$Hg(ad) + M_xO_y \rightarrow HgO(ad) + M_xO_{y-1} \quad (3)$$

$$M_xO_{y-1} + 1/2O_2 \rightarrow M_xO_y \quad (4)$$

$$HgO(ad) + M_xO_y \rightarrow HgM_xO_{y+1} \quad (5)$$

where M_xO_y can be seen as Fe_xO_y, Mn_xO_y, and Ce_xO_y. The existence of M_xO_{y-1} in the catalyst implies the formation of oxygen vacancy, which can be the adsorption sites for gas phase oxygen to form active oxygen over the catalyst surface. In this work, Mn_xO_y and Ce_xO_y were the active components and played an important role in the adsorption of Hg^0. In the adsorption process, Hg^0 adsorption on Ce-Mn-Fe/GO-x (x = 0, 10%, 20%, 30%) is a dynamic process: First, the Hg^0(g) forms Hg(ads), and then, Mn_xO_y and Ce_xO_y offer lattice oxygen for the oxidation of Hg(ads).

2.6. Regeneration

The most outstanding of the above samples is Ce-Mn-Fe/GO-20%. After 6 h, the Hg^0 and NO_x removal efficiencies reduced to 54% and 46%, respectively. To explore the active regeneration of the catalyst, the methods of heating to 400 °C in an atmosphere of nitrogen was employed. However, as Figure 10 shows, with the increase of cycling time, the Hg^0 and NO_x removal performance decreased slightly. After the third circulation, the regeneration capacity of Hg^0 and NO_x removal reached 85%, so that the regeneration capacity of Ce-Mn-Fe/GO-x highlights its potential applications in the future.

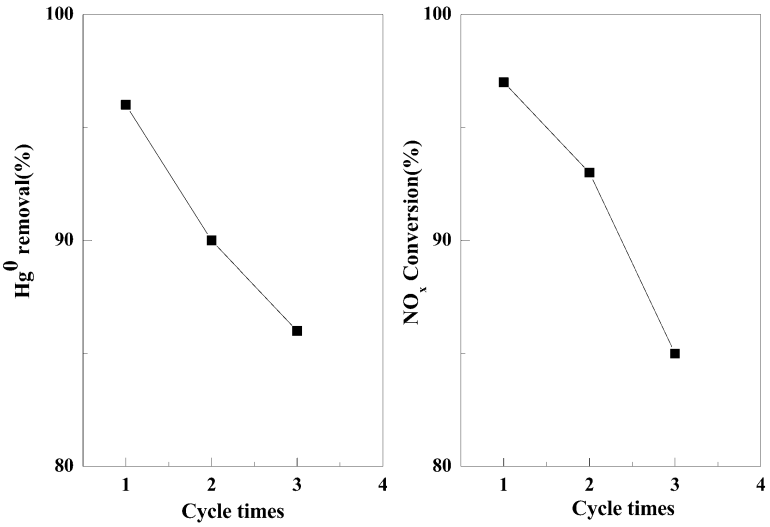

Figure 10. Regeneration performance of the sorbent for Hg^0 and NO_x removal efficiency.

3. Experimental

3.1. Catalyst Preparation

The title composites of Ce-Mn-Fe/GO-x catalysts were synthesized by a hydrothermal method. The commercially available chemicals are reagent grade, and the GO was purchased from Qingdao Tianhe Graphite, Qingdao, China. A mixture of $Ce(NO_3)_3{\cdot}6H_2O$, $Mn(NO_3)_2{\cdot}6H_2O$, and $Fe(NO_3)_3{\cdot}9H_2O$, with a molar ratio of 1:1:1(0.001 mol $Ce(NO_3)_3{\cdot}6H_2O$, and 0.001 mol $Mn(NO_3)_2{\cdot}6H_2O$, 0.001 mol $Fe(NO_3)_3{\cdot}9H_2O$), respectively, was employed. The reagents were dissolved in 70 mL deionized water and placed inside a 100 mL autoclave with 0, 0.1, 0.2, and 0.3 g GO, respectively. Then, the autoclave was heated inside a furnace to 180 °C for 24 h and slowly cooled to room temperature at a rate of 10 °C/h. Further, the precursor was washed using deionized water five times, then calcined at 500 °C under N_2 for 3 h. Finally, highly dispersed Ce-Mn-Fe-O nanoparticles were anchored on the surfaces of the GO, and the Ce-Mn-Fe/GO-x (x = 0%, 10%, 20%, 30%, CeO_x 0.17 g, MnO_x 0.68 g, FeO_x 0.15 g) composites were obtained, where x is the mass percentages of GO in the composite.

3.2. Material Characterizations

The surface morphology was characterized using a scanning electron microscope (SEM:DESK V, Denton Vacuum, Cherry Hill, NJ, USA). The X-ray diffraction data were obtained while using a Bruker D2 PHASER diffractometer (Bruker Corp, Billerica, MA, USA), equipped with an incident beam monochromator set for Cu Kα radiation (λ = 1.5418 Å). Diffraction patterns were taken from 10° to 80° (2θ), with a scan step width of 0.02°, and a fixed counting time of 1 s/step. The surface property was analyzed by X-ray photoelectron spectroscopy (XPS), while using a VG Multilab 2000 X-ray photoelectron spectrometer (Thermo Fisher Scientific, Waltham, MA, USA), with Al Kα as the excitation source. The C_{1s} line at 284.8 eV was taken as a reference for binding energy calibration, and experimental data were fitted with the Gaussian-Lorentzian mixed function, as implemented in the XPS software. The specific surface areas of the catalysts were determined while using the BET method, the pore volume and pore size were calculated by the Brunauer-Emmett-Teller (BET) method (Quantachrome, Boynto Beach, FL, USA). The temperature-programmed reduction (H_2-TPR) experiments were tested by Chembet Pulsar TPR/TPD 2139 (Quantachrome, Boynto Beach, FL, USA) to study the reducibility of catalysts.

3.3. Hg^0 Removal Test

A lab-scale fixed-bed (the inner diameter, height, and thickness is 25 mm, 300 mm, and 2 mm, respectively) reaction system was assembled to evaluate the performance of the catalytic oxidation of Hg^0, as shown in Figure 11. In each test, a 2.4 mL sample with a 40–60 mesh size was loaded in the reactor, which was placed in the center of a temperature-programmable electric furnace. A Hg^0 permeation tube, loaded in a U-shaped glass tube, was used to generate Hg^0 vapor carried by pure N_2. The concentration of the Hg^0 feed (45 $\mu g \cdot m^{-3}$) was provided steadily, and the concentration of Hg^0 was measured while using a Thermo Fisher mercury continuous emission monitoring system (Hg^0 CEMS). Other simulated gases, including NO, O_2, SO_2, H_2O, and NH_3, were introduced into the gas mixer at constant flow rates, controlled by mass flow controllers. The total flow rate was kept at 2 L/min for the accuracy of the experiment, and the calculated space velocity for the tests was 30,000 h^{-1}. In every test, the mercury inlet gas stream bypassed the reaction bed and passed into the analytical system, until the desired inlet mercury concentration was established, and the reaction temperature was controlled from 100 to 400 °C by a temperature-programmed control. The outlet Hg^0 concentration was measured at the condition of the gas flow, which was passed through the reactor. Hence, the Hg^0 removal efficiency (E_{oxi}) was calculated according to Equation (6):

$$E_{oxi} = \frac{Hg^0_{in} - Hg^0_{out}}{Hg^0_{in}} \times 100\% \quad (6)$$

where Hg^0_{in} and Hg^0_{out} are the inlet and outlet of Hg^0 concentration, respectively, which were measured by CEMS.

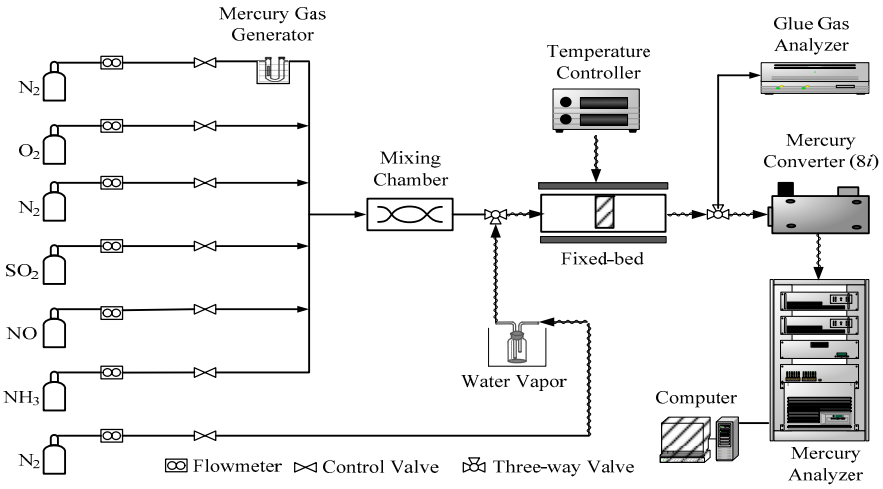

Figure 11. Schematic diagram of the experimental setup.

3.4. NH_3-SCR Catalytic Activity Measurement

The NH_3-SCR of NO_x experiments were performed according to the procedures employed in the Hg^0 oxidation tests (Figure 11). The 2.4 mL sample was placed into the reactor, and the reactant gas typically consisted of 800 ppm NO, 800 ppm NH_3, and 6% O_2. Moreover, N_2 was employed as the balanced atmosphere in the reaction system. The reaction temperature was controllable from 100 to 400 °C at a heating rate of 5 °C/min. An infrared gas analyzer (GASMET DX4000, Temet Instruments Oy, Helsinki, Finland) was used to check for a gas component in the outlet of the flue gas. Conversion was calculated according to Equation (7):

$$\eta = \frac{[NO_x]_{in} - [NO_x]_{out}}{[NO_x]_{in}} \times 100\% \quad (7)$$

where $[NO_x]_{in}$ and $[NO_x]_{out}$ refer to the inlet and outlet of NO_x concentration, respectively. η is the reduction efficiency of NO_x. All the concentrations were measured by an infrared gas analyzer.

4. Conclusions

The catalysts of Ce-Mn-Fe/GO-x (x = 0, 10%, 20%, 30%) have been successfully obtained via a hydrothermal method. Ce-Mn-Fe/GO-20% shows the best performance in Hg^0 and NO_x removal in simulated flue gas. The better performance of Ce-Mn-Fe/GO-20% in capturing Hg^0 and NO_x than other comparative composites is owing to the highly dispersed Fe-Mn-Ce-O particles on the GO nanosheets. Besides, the effect factors in Hg^0 removal are determined by O_2 and SO_2 + O_2, which are beneficial for Hg^0 removal, but the SO_2 has an inhibitory effect on Hg^0 and NO_x removal. Further, NO shows an inhibitory effect on Hg^0 removal, and this inhibitory effect can be slightly reduced by adding 6% O_2 into the flue gas. The negative effect of water vapor results from the adsorption of H_2O on the catalysts, which has a further effect on Hg^0 oxidation and NO_x reduction, and the effect can recover soon after cutting off the H_2O injection. However, the active metal oxides that were loaded on GO have better water resistance than the compared catalysts. The catalyst not only exhibited a superior performance in Hg^0 oxidation, but showed itself to be an ideal material for NO_x reduction within the same temperature range from 170 to 250 °C. Thus, Ce-Mn-Fe/GO-20% has potential applications both in the field of Hg^0 oxidation and NO_x reduction.

Supplementary Materials: The following are available online at http://www.mdpi.com/2073-4344/8/9/399/s1, Figure S1: The element contents on the surface of graphene (EDS) and SEM images of Ce-Mn-Fe/GO0, Figure S2: The element contents on the surface of graphene (EDS) and SEM images of Ce-Mn-Fe/GO-0.1, Figure S3:The element contents on the surface of graphene (EDS) and SEM images of Ce-Mn-Fe/GO-0.3, Figure S4: NO_x conversion as a function of reaction temperature over the Ce-Mn-Fe/GO-x (x = 0, 0.1, 0.3) samples. (Reaction conditions: 800 ppm NO, 800 ppm NH_3, 6% O_2 and N_2 balance, GHSV = 30,000 h^{-1}).

Author Contributions: D.A. and Y.D. conceived and designed the experiments; D.A. conducted the experiments and wrote the paper; X.Z. analyzed the data; X.C. software and checked the paper.

Funding: This research was funded by Foundation of State Key Laboratory of Coal Combustion (FSKLCCA1603).

Acknowledgments: The authors express thanks for the support of Foundation of State Key Laboratory of Coal Combustion (FSKLCCA1603).

Conflicts of Interest: The authors declare no conflict of interest.

References

1. Chen, D.Y.; Zhao, S.J.; Qu, Z.; Yan, N.Q. Cu-BTC as a novel material for elemental mercury removal from sintering gas. *Fuel* **2018**, *217*, 297–305. [CrossRef]
2. Zhao, B.; Yi, H.H.; Tang, X.L.; Li, Q.; Liu, D.D.; Gao, F.Y. Copper modified activated coke for mercury removal from coal-fired flue gas. *Chem. Eng. J.* **2016**, *286*, 585–593. [CrossRef]
3. Pavlish, J.H.; Sondreal, E.A.; Mann, M.D.; Olson, E.S.; Galbreath, K.C.; Laudal, D.L.; Benson, S.A. Status review of mercury control options for coal-fired power plants. *Fuel Process. Technol.* **2003**, *82*, 89–165. [CrossRef]
4. Xu, W.; Shao, M.; Yang, Y.; Liu, R.; Wu, Y.; Zhu, T. Mercury emission from sintering process in the iron and steel industry of china. *Fuel Process. Technol.* **2017**, *159*, 340–344. [CrossRef]
5. Driscoll, C.T.; Mason, R.P.; Chan, H.M.; Jacob, D.J.; Pirrone, N. Mercury as a global pollutant: Sources, pathways, and effects. *Environ. Sci. Technol.* **2013**, *47*, 4967–4983. [CrossRef] [PubMed]
6. Zhang, Y.; Wang, C.B.; Liu, H.M. Experiment and mechanism research on gas-phase As_2O_3 adsorption of Fe_2O_3/γ-Al_2O_3. *Fuel* **2016**, *181*, 1034–1040. [CrossRef]
7. Xu, M.H.; Qiao, Y.; Zhang, C.G.; Li, L.C.; Liu, J. Modeling of homogeneous mercury speciation using detailed chemical kinetics. *Combust. Flame.* **2003**, *132*, 208–218. [CrossRef]
8. Zhang, S.B.; Zhao, Y.C.; Yang, J.P.; Zhang, Y.; Sun, P.; Yu, X.H.; Zhang, J.Y.; Zheng, C.G. Simultaneous NO and mercury removal over MnO_x/TiO_2 catalyst in different atmospheres. *Fuel Process. Technol.* **2017**, *166*, 282–290. [CrossRef]

9. Yang, J.P.; Zhao, Y.C.; Chang, L.; Zhang, J.Y.; Zheng, C.G. Mercury adsorption and oxidation over cobalt oxide loaded magnetospheres catalyst from fly ash in oxyfuel combustion flue gas. *Environ. Sci. Technol.* **2015**, *49*, 8210–8218. [CrossRef] [PubMed]
10. Li, Y.N.; Duan, Y.F.; Wang, H.; Zhao, S.L.; Chen, M.M.; Liu, M.; Wei, H.Q. Effects of acidic gases on mercury adsorption by activated carbon in simulated oxy-fuel combustion flue gas. *Energy Fuels* **2017**, *31*, 9745–9751. [CrossRef]
11. Pacyna, E.G.; Pacyna, J.M.; Sundseth, K.; Munthe, J.; Kindbom, K.; Wilson, S.; Steenhuisen, F.; Maxson, P. Global emission of mercury to the atmosphere from anthropogenic sources in 2005 and projections to 2020. *Atmos. Environ.* **2010**, *44*, 2487–2499. [CrossRef]
12. Cai, J.H.; Jia, C.Q. Mercury removal from aqueous solution using coke-derived sulfur-impregnated activated carbons. *Ind. Eng. Chem. Res.* **2010**, *49*, 2716–2721. [CrossRef]
13. Xu, W.Q.; Wang, H.R.; Zhu, T.Y.; Kuang, J.Y.; Jing, P.F. Mercury removal from coal combustion flue gas by modified fly ash. *J. Environ. Sci.* **2013**, *25*, 393–398. [CrossRef]
14. Zhang, M.Z.; Wang, P.; Dong, Y.; Sui, H.; Xiao, D.D. Study of elemental mercury oxidation over an SCR catalyst with calcium chloride addition. *Chem. Eng. J.* **2014**, *253*, 243–250. [CrossRef]
15. Straube, S.; Hahn, T.; Koeser, H. Adsorption and oxidation of mercury in tail-end SCR-DeNO$_x$ plants-bench scale investigations and speciation experiments. *Appl. Catal. B Environ.* **2008**, *79*, 286–295. [CrossRef]
16. Mei, Z.J.; Shen, Z.M.; Zhao, Q.J.; Wang, W.H.; Zhang, Y.J. Removal and recovery of gas-phase element mercury by metal oxide-loaded activated carbon. *J. Hazard. Mater.* **2008**, *152*, 721–729. [CrossRef] [PubMed]
17. Pavlish, J.H.; Hamre, L.L.; Zhuang, Y. Mercury control technologies for coal combustion and gasification systems. *Fuel* **2010**, *89*, 838–847. [CrossRef]
18. Li, C.W.; Zhang, A.C.; Zhang, L.X.; Song, J.; Su, S.; Sun, Z.J.; Xiang, J. Enhanced photocatalytic activity and characterization of magnetic Ag/BiOI/ZnFe$_2$O$_4$ composites for Hg^0 removal under fluorescent light irradiation. *Appl. Surf. Sci.* **2018**, *433*, 914–926. [CrossRef]
19. Gao, Y.S.; Zhang, Z.; Wu, J.W.; Duan, L.H.; Umar, A.; Sun, L.Y.; Guo, Z.H.; Wang, Q. A critical review on the heterogeneous catalytic oxidation of elemental mercury in flue gases. *Environ. Sci. Technol.* **2013**, *47*, 10813–10823. [CrossRef] [PubMed]
20. Li, H.L.; Zhu, L.; Wu, S.K.; Liu, Y.; Shih, K. Synergy of CuO and CeO$_2$ combination for mercury oxidation under low-temperature selective catalytic reduction atmosphere. *Int. J. Coal Geol.* **2017**, *170*, 69–76. [CrossRef]
21. Liu, R.; Xu, W.; Tong, L.; Zhu, T. Role of NO in Hg0 oxidation over a commercial selective catalytic reduction catalyst V$_2$O$_5$–WO$_3$/TiO$_2$. *J. Environ. Sci.* **2015**, *38*, 126–132. [CrossRef] [PubMed]
22. Du, W.; Yin, L.B.; Zhuo, Y.Q.; Xu, Q.S.; Zhang, L.; Chen, C.H. Performance of CuO$_x$-neutral Al$_2$O$_3$ sorbents on mercury removal from simulated coal combustion flue gas. *Fuel Process. Technol.* **2015**, *131*, 403–408. [CrossRef]
23. Chen, G.Q.; Gao, J.; Xu, L.; Fu, X.; Yin, Y.; Wu, S.; Qin, Y. Optimizing conditions for preparation of MnO$_x$/RHA catalyst particle for the catalytic oxidation of No. *Adv. Powder Technol.* **2012**, *23*, 256–263. [CrossRef]
24. He, C.; Shen, B.X.; Chen, J.H.; Cai, J. Adsorption and oxidation of elemental mercury over Ce-MnO$_x$/Ti-PILCs. *Environ. Sci. Technol.* **2014**, *48*, 7891–7898. [CrossRef] [PubMed]
25. Wu, S.K.; Li, H.L.; Li, L.Q.; Wu, C.Y.; Zhang, J.Y.; Shih, K. Effects of flue-gas parameters on low temperature NO reduction over a Cu-promoted CeO$_2$–TiO$_2$ catalyst. *Fuel* **2015**, *159*, 876–882. [CrossRef]
26. Zhang, A.C.; Zhang, Z.H.; Chen, J.J.; Sheng, W.; Sun, L.S.; Xiang, J. Effect of calcination temperature on the activity and structure of MnO$_x$/TiO$_2$ adsorbent for Hg0 removal. *Fuel Process. Technol.* **2015**, *135*, 25–33. [CrossRef]
27. Liu, T.; Man, C.Y.; Guo, X.; Zheng, C.G. Experimental study on the mechanism of mercury removal with Fe$_2$O$_3$. *Fuel* **2016**, *173*, 209–216. [CrossRef]
28. Li, H.L.; Wu, C.Y.; Li, Y.; Zhang, J.Y. Superior activity of MnO$_x$-CeO$_2$/TiO$_2$ catalyst for catalytic oxidation of elemental mercury at low flue gas temperatures. *Appl. Catal. B Environ.* **2012**, *111–112*, 381–388. [CrossRef]
29. Qi, G.; Yang, R.T. Characterization and FTIR studies of MnO$_x$-CeO$_2$ catalyst for low-temperature selective catalytic reduction of NO with NH$_3$. *J. Phy. Chem. B.* **2004**, *108*, 15738–15747. [CrossRef]
30. Yang, S.J.; Guo, Y.F.; Yan, N.Q.; Qu, Z.; Xie, J.K.; Yang, C.; Jia, J.P. Capture of gaseous elemental mercury from flue gas using a magnetic and sulfur poisoning resistant sorbent Mn/γ-Fe$_2$O$_3$ at lower temperatures. *J. Hazard. Mater.* **2011**, *186*, 508–515. [CrossRef] [PubMed]

31. Xu, H.M.; Qu, Z.; Zong, C.X.; Huang, W.J.; Quan, F.Q.; Yan, N.Q. MnO_x/graphene for the catalytic oxidation and adsorption of elemental mercury. *Environ. Sci. Technol.* **2015**, *49*, 6823–6830. [CrossRef] [PubMed]
32. Li, J.R.; Chen, J.S.; Yu, Y.K.; He, C. Fe–Mn–Ce/ceramic powder composite catalyst for highly volatile elemental mercury removal in simulated coal-fired flue gas. *J. Ind. Eng. Chem.* **2015**, *25*, 352–358. [CrossRef]
33. Novoselov, K.S.; Geim, A.K.; Morozov, S.V.; Jiang, D.; Zhang, Y.; Dubonos, S.V.; Grigorieva, I.V.; Firsov, V.V. Electric field effect in atomically thin carbon films. *Science* **2004**, *306*, 666–669. [CrossRef] [PubMed]
34. Georgakilas, V.; Otyepka, M.; Bourlinos, A.B.; Chandra, V.; Kim, N.; Kemp, K.C.; Hobza, P.; Zboril, R.; Kim, K.S. Functionalization of graphene: covalent and non-covalent approaches, derivatives and applications. *Chem. Rev.* **2012**, *112*, 6156–6214. [CrossRef] [PubMed]
35. Li, H.N.; Zhu, M.Y.; Chen, W.; Xu, L.; Wang, K. Non-light-driven reduced graphene oxide anchored TiO_2 nanocatalysts with enhanced catalytic oxidation performance. *J. Colloid Interface Sci.* **2017**, *507*, 35–41. [CrossRef] [PubMed]
36. Qu, J.Y.; Shi, L.; He, C.X.; Gao, F.; Li, B.B.; Zhou, Q.; Hu, H.; Shao, G.H.; Wang, X.Z.; Qiu, J.S. Highly efficient synthesis of graphene/MnO_2 hybrids and their application for ultrafast oxidative decomposition of methylene blue. *Carbon* **2014**, *66*, 485–492. [CrossRef]
37. Qiao, S.H.; Chen, J.; Li, J.F.; Qu, Z.; Liu, P.; Yan, N.Q.; Jia, J.P. Adsorption and catalytic oxidation of gaseous elemental mercury in flue gas over MnO_x/alumina. *Ind. Eng. Chem. Res.* **2009**, *48*, 3317–3322. [CrossRef]
38. Wang, J.G.; Yi, H.H.; Tang, X.L.; Zhao, S.Z.; Gao, F.Y.; Yang, Z.Y. Oxygen plasma-catalytic conversion of NO over MnO_x: Formation and reactivity of adsorbed oxygen. *Catal. Commun.* **2017**, *100*, 227–231. [CrossRef]
39. Reddy, B.M.; Khan, A.; Yamada, Y.; Kobayashi, T.; Loridant, S.; Volta, J.-C. Structural characterization of CeO_2-TiO_2 and V_2O_5/CeO_2-TiO_2 catalysts by raman and XPS techniques. *J. Phys. Chem. B* **2003**, *107*, 5162–5167. [CrossRef]
40. Zhou, Z.J.; Liu, X.W.; Hu, Y.C.; Liao, Z.Q.; Cheng, S.; Xu, M.H. An efficient sorbent based on $CuCl_2$ loaded CeO_2-ZrO_2 for elemental mercury removal from chlorine-free flue gas. *Fuel* **2018**, *216*, 356–363. [CrossRef]
41. Ding, Z.Y.; Li, L.X.; Wade, D.; Gloyna, E.F. Supercritical water oxidation of NH_3 over a MnO_2. *Ind. Eng. Chem. Res.* **1998**, *37*, 1707–1716. [CrossRef]
42. Li, H.H.; Wang, Y.; Wang, S.K.; Wang, X.; Hu, J.J. Removal of elemental mercury in flue gas at lower temperatures over Mn-Ce based materials prepared by co-precipitation. *Fuel* **2017**, *208*, 576–586. [CrossRef]
43. Wang, L.Y.; Cheng, X.X.; Wang, Z.Q.; Ma, C.Y.; Qin, Y.K. Investigation on Fe-Co binary metal oxides supported on activated semi-coke for NO reduction by Co. *Appl. Catal. B Environ.* **2017**, *201*, 636–651. [CrossRef]
44. Xing, L.L.; Xu, Y.L.; Zhong, Q. Mn and Fe modified fly ash as a superior catalyst for elemental mercury capture under air conditions. *Energy Fuels* **2012**, *26*, 4903–4909. [CrossRef]
45. Kang, M.; Park, E.D.; Kim, J.M.; Yie, J.E. Manganese oxide catalysts for NO_x reduction with NH_3 at low temperatures. *Appl. Catal. A Gen.* **2007**, *327*, 261–269. [CrossRef]
46. Dupin, J.C.; Gonbeau, D.; Vinatier, P.; Levasseur, A. Systematic XPS studies of metal oxides, hydroxides and peroxides. *Phys. Chem. Chem. Phys.* **2000**, *2*, 1319–1324. [CrossRef]
47. Zhao, Y.C.; Zhang, J.Y.; Tian, C.; Li, H.L.; Shao, X.Y.; Zheng, C.G. Mineralogy and chemical composition of high-calcium fly ashes and density fractions from a coal-fired power plant in china. *Energy Fuels* **2010**, *24*, 834–843. [CrossRef]
48. Gao, G.; Shi, J.W.; Liu, C.; Gao, C.; Fan, Z.Y.; Niu, C.M. Mn/CeO_2 catalysts for SCR of NO_x with NH3: Comparative study on the effect of supports on low-temperature catalytic activity. *Appl. Surf. Sci.* **2017**, *411*, 338–346. [CrossRef]
49. Ndifor, E.N.; Garcia, T.; Solsona, B.; Taylor, S.H. Influence of preparation conditions of nano-crystalline ceria catalysts on the total oxidation of naphthalene, a model polycyclic aromatic hydrocarbon. *Appl. Catal. B: Environ.* **2007**, *76*, 248–256. [CrossRef]
50. Zhang, X.Y.; Ma, C.Y.; Cheng, X.X.; Wang, Z.Q. Performance of Fe-Ba/ZSM-5 catalysts in NO + O_2 adsorption and NO + CO reduction. *Int. J. Hydrogen Energy* **2017**, *42*, 7077–7088. [CrossRef]
51. Zhang, A.C.; Xing, W.B.; Zhang, Z.H.; Meng, F.M.; Liu, Z.C.; Xiang, J.; Sun, L.S. Promotional effect of SO_2 on CeO_2-TiO_2 material for elemental mercury removal at low temperature. *Atmos. Pollut. Res.* **2016**, *7*, 895–902. [CrossRef]
52. Busca, G.; Lietti, L.; Ramis, G.; Berti, F. Chemical and mechanistic aspects of the selective catalytic reduction of NO_x by ammonia over oxide catalysts: A review. *Appl. Catal. B Environ.* **1998**, *18*, 1–36. [CrossRef]

53. Zheng, Y.J.; Jensen, A.D.; Windelin, C.; Jensen, F. Review of technologies for mercury removal from flue gas from cement production processes. *Prog. Energy Combust. Sci.* **2012**, *38*, 599–629. [CrossRef]
54. Liu, Z.M.; Liu, H.Y.; Zeng, H.; Xu, Q. A novel Ce-Sb binary oxide catalyst for the selective catalytic reduction of NO_x with NH_3. *Catal. Sci. Technol.* **2016**, *6*, 8063–8071. [CrossRef]
55. Miser, D.E.; Shin, E.J.; Hajaligol, M.R.; Rasouli, F. HRTEM characterization of phase changes and the occurrence of maghemite during catalysis by an iron oxide. *Appl. Catal. A Gen.* **2004**, *258*, 7–16. [CrossRef]